HiSST: 3rd International Conference on
High-Speed Vehicle Science Technology
14 -19 April 2024, Busan, Korea

Numerical Study of Turbulent Combustion in High Mach Number Scramjet Engine with Thermodynamic Non-equilibrium Effect

Hai Feng[1], Tai Jin[1], Kun Wu[2]*

Abstract

Thermodynamic non-equilibrium effect has a significant impact on hypersonic aircraft and must be taken into consideration in numerical computations. Numerical simulations of a Mach 12 flight condition scramjet engine were conducted using both the thermodynamic equilibrium model and Park's dual-temperature non-equilibrium model. The results indicate that, compared to equilibrium state calculations, non-equilibrium effects lead to a forward shift in the wave system position, resulting in a significant increase in peak pressure between shock waves, with a more pronounced impact on the cold flow. The non-equilibrium Ttr temperature field is generally similar to the equilibrium state. Thermodynamic non-equilibrium effects lead to a slight increase in Ttr. In the non-equilibrium state, the combustion efficiency at the outlet section of the combustion chamber is lower, indicating that thermodynamic non-equilibrium effects weaken the extent of the reaction.

Keywords: *hypersonic; thermodynamic non-equilibrium; scramjet; wave structure; combustion efficiency*

Nomenclature

c_p – Pressure coefficient
Ma – Mach
P – Pressure
T – Temperature
U – Velocity
URANS – Unsteady Reynolds Average Navier-Stokes
V-T – Vibrational-translational
y+ – Y-plus
ρ – Density
Ω – Damkhöler number
τ – Characteristic Time

1. Introduction

In hypersonic flow, moving gas molecules undergo compression due to shock waves and viscous drag, converting kinetic energy into internal energy, thereby forming high-temperature regions behind shock waves or within boundary layers. The extremely high temperature intensifies the thermal motion of gas molecules, leading to excitation of molecular vibrational and electronic energies [1]. Gas molecules may dissociate or even ionize, causing the breakdown of the assumption of perfect gas behavior, known as the high-temperature (real) gas effect.

The high-temperature gas effect [2] is the result of intense thermal motion and continuous collisions among gas molecules under high-temperature conditions. This process, after a certain period, will reach a stable equilibrium state, where macroscopically, there is no further change in thermophysical and chemical properties. However, in certain cases, gas molecules may not have sufficient time to reach an equilibrium state. For instance, at high Mach numbers, the residence time of the airflow is much shorter than the time required to reach equilibrium, resulting in the gas being in a non-equilibrium state during the flow process [3]. Thermodynamic non-equilibrium refers to the delayed variation of the local gas flow's vibrational temperature compared to its translational temperature. Because temperature changes

[1] *School of Aeronautics and Astronautics, Zhejiang University, Hangzhou, 310027, China, jintai@zju.edu.cn*
[2] *Institute of Mechanics, Chinese Academy of Sciences, Beijing, 100190, China, wukun@imech.ac.cn*

are the trigger, this phenomenon is more likely to occur in regions with large temperature gradients, such as shock waves, expansion waves, and flames. The thermodynamic Damkhöler number Ω_t serves as a criterion, where $\Omega_t = \tau_{res} / \tau_t$, with τ_{res} being the residence time and τ_t being the relaxation time for vibrational energy equilibrium. $\Omega_t >> 1$ indicates thermodynamic equilibrium, $\Omega_t << 1$ indicates vibrational temperature freeze, and $\Omega_t \approx 1$ indicates thermodynamic non-equilibrium. Similarly, for chemical non-equilibrium, the criterion is the Damkhöler number Ω_c. $\Omega_c = \tau_{res} / \tau_{m\text{-}k}$, with τ_{res} being the residence time and $\tau_{m\text{-}k}$ being the time required for mixing and chemical reactions. $\Omega_c >> 1$ represents chemical equilibrium flow, $\Omega_c << 1$ represents frozen composition flow, and $\Omega_c \approx 1$ represents chemical non-equilibrium flow [4].

According to the typical flow characteristic diagrams compiled by Longo [5] and others, as well as Anna [6], during re-entry into the atmosphere, it is understood that the thermochemical state of the gas is correlated with two factors: flight speed and flight altitude. Flight speed primarily determines the thermodynamic state, whether vibrational energy is excited, and whether dissociation occurs. Meanwhile, flight altitude primarily determines whether the flow is in thermodynamic equilibrium, non-equilibrium, or frozen state. At lower flight speeds, the gas can be considered an ideal gas, where only the translational and rotational energies of gas molecules need to be considered. As the flight speed increases further, the gas temperature rises, and after reaching a certain level, the vibrational energy of gas molecules becomes excited. With further increases in flight speed, oxygen molecules in the air begin to dissociate. Moreover, as the flight speed continues to increase, nitrogen gas will also undergo dissociation and ionization reactions. When an aircraft flies in the atmosphere below 30 km, due to the higher density of gas molecules, thermochemical reactions can swiftly complete, and the flow remains in equilibrium. However, at altitudes exceeding 60 km, the gas becomes rarefied in the atmospheric layer, reducing the frequency of molecular collisions and thus slowing down thermochemical reaction rates, resulting in the flow being in a non-equilibrium state.

Under high-temperature conditions, non-equilibrium effects have a significant impact on the flow field and must be considered in numerical calculations. For instance, during the re-entry of a spacecraft into the atmosphere, when the aircraft is trimmed, using an ideal gas model to simulate the flow field would inaccurately calculate the distribution of mass, momentum, and energy in the flow field. Consequently, it would fail to provide accurate pitch moment and angle of attack trimming parameters. Numerous studies have demonstrated that high-temperature chemical reaction flows have a significant impact on the lift, drag, and moments of hypersonic vehicles. Another major aspect of non-equilibrium effects is the high heat transfer rate generated on surfaces, which can lead to severe aerodynamic heating and material erosion. This phenomenon is crucial for the design of spacecraft and engines [7].

To summarize, thermochemical non-equilibrium effects have a significant impact on hypersonic aircraft, but related research remains limited and insufficient. In this study, the simulated Mach number is 12, with an inlet velocity of 3600 m/s for a scramjet engine, involving hydrogen combustion reactions where vibrational energy is excited at high Mach numbers, necessitating consideration of thermodynamic non-equilibrium. Additionally, due to the rapid hydrogen combustion reaction, the Damkohler number is far greater than 1, indicating a chemically equilibrium flow. Numerical simulations of the flow field in a supersonic combustion ramjet engine, which is introduced by Bricalli et al. [8], are conducted using both thermodynamic equilibrium and Park's dual-temperature non-equilibrium models. The aim is to analyze the effects of thermodynamic non-equilibrium on the characteristics of hypersonic scramjet engines.

2. The physical model and numerical methods.

2.1. Flow solver and models

The numerical simulation in this paper is conducted using the hy2Foam solver, developed based on the open-source OpenFOAM platform. This solver, derived from rhoCentralFoam and reactingFoam, couples thermodynamic non-equilibrium and chemical non-equilibrium models. It is capable of computing complex non-equilibrium flow phenomena, particularly addressing high-temperature gas effects [9]. Traditionally, the computation of continuous transient hypersonic reacting flows employs the non-equilibrium Navier–Stokes–Fourier (NSF) equations [10]. Thermodynamic non-equilibrium is modeled using Park's dual-temperature model, which introduces the vibration temperature T_v and the vibration energy equation. The energy exchange between translational-rotational and vibrational modes in the

vibration energy equation is determined by the Landau-Teller equation [11]. In contrast, the single-temperature model of thermodynamic equilibrium assumes $T_v = T_{tr}$ and no longer solves the vibration energy equation, but the total energy still includes vibration energy.

2.2. Turbulence and combustion models

In this study, URANS simulation is employed, and the Shear Stress Transport (SST) k-ω model is used to simulate turbulence. This turbulence model has been demonstrated to accurately capture phenomena in supersonic flows, such as shock/boundary layer interactions (SBLI) and the mixing process of fuel injection into supersonic crossflows [12]. Combustion is simulated using a 10-species 21-step finite-rate reaction model developed by CONAIRE [13].

2.3. Numerical settings

The computational domain is discretized using a finite volume method with a cell-centered storage structure. The time integration is performed using a first-order explicit Euler method. The convection fluxes are computed using a second-order central differencing scheme combined with limitedLinear1 interpolation for left and right states. Additionally, the Kurganov scheme is utilized to compute hyperbolic conservation fluxes. Diffusion fluxes are discretized using a modified central differencing scheme. The PBiCGStab method combined with DILU preconditioning technique is employed to solve all algebraic equations, with a convergence residual within each time step set to 1×10^{-12}. In the computations, the maximum Courant number is set to 0.5, corresponding to a stable time step of the order of 4×10^{-9}s.

2.4. Geometry and boundary conditions

Table 1. Geometric parameters of the scramjet engine

W_I	θ_I	x_j	L_I	L_C	L_N	H_C	θ_N	H_N
25mm	13°	37mm	122mm	328mm	410mm	12.5mm	12°	100mm

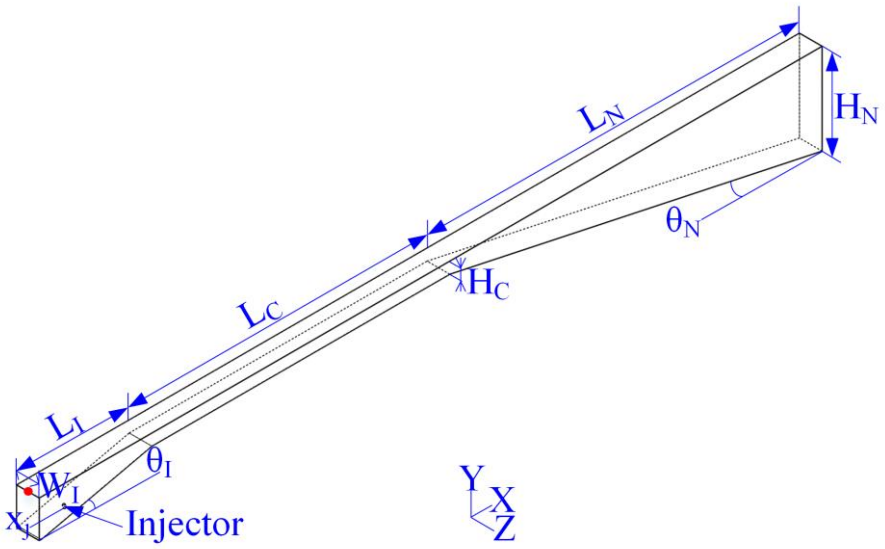

Fig. 1 Physical model of the scramjet engine

Table 1 and Fig. 1 present the physical model and geometric parameters of the simulated three-dimensional scramjet engine. The red dot in Fig. 1 is designated as the origin. Boundary conditions for both thermodynamic equilibrium and non-equilibrium states are provided in Table 2. The preheated air accelerates to Mach 12 before entering the engine inlet. The molar fractions of each component are 21% O2 and 79% N2. Hydrogen fuel is injected into the fuel nozzle at Mach 1 speed. To compare with the results of Bricalli et al. [8], the equivalence ratio is set to 1. The initial conditions for thermodynamic non-equilibrium are maintained consistent with the total enthalpy of the thermally equilibrium state [14].

Table 2. Inflow initial conditions

Case	Patch	Velocity U/ m·s^{-1}	Static Pressure P_s/Pa	Trans-rotational Temperature T_{tr}/K	Vibrational Temperature T_v/K
Thermodynamic equilibrium	Inlet	3600	1008	227	-
	Inletfuel	1208	451954.6	249	-
Non-equilibrium	Inlet	3600	1008	226.93	226.93
	Inletfuel	1208	451954.6	248.99	248.99

All inlets use Dirichlet boundaries with a turbulence intensity of 5%. Outlet variables are obtained from internal second-order interpolation. The upper wall is set as a symmetric boundary, and the lower wall is a 300K isothermal wall. The computational domain grid is shown in Fig. 2. To reduce computational load, the spanwise direction is reduced to 1/4 of the original size (25 mm). Only one fuel injector is retained, and symmetric boundaries are set on the front and back walls. The combustion chamber walls, fuel jet, and transition regions are all refined using expansion grids. The first layer grid height at the wall is 0.03 mm, aiming for a y+ value around 250, which, combined with the k-ω SST model, meets the computational requirements.

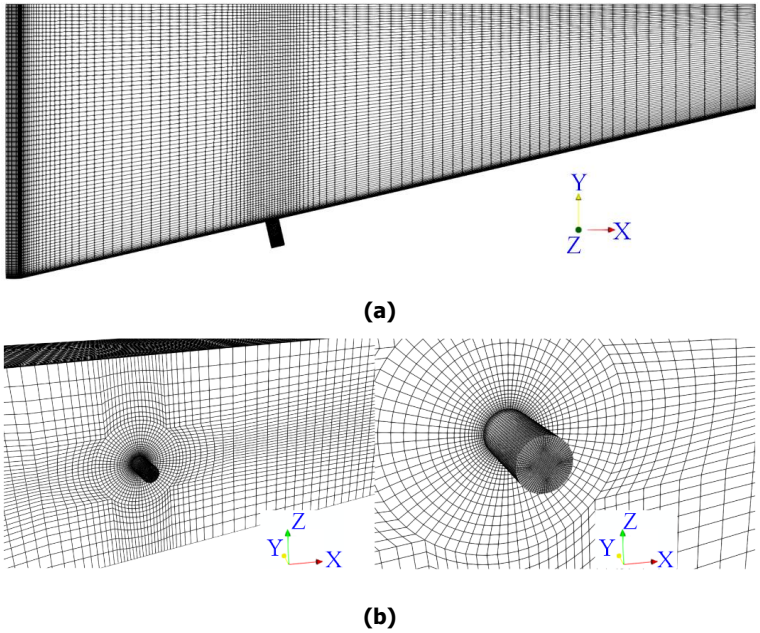

Fig. 2 The computational mesh: (a) front view, (b) zoom-in view of the fuel injector

2.5. Verification of computational methods

The computational methods in this paper are validated using the results of Bricalli et al. [15] for a scramjet engine operating under Ma = 10 flow conditions. The inflow parameters are as shown in Table 3:

Table 3. Boundary conditions for air and fuel stream

Patch	Mach	Velocity U/ m·s^{-1}	Static Pressure P_s/Pa	Trans-rotational Temperature T_{tr}/K
Inlet	10	3000	1450	227
Inletfuel	1	1208	541778	249

A comparison of the pressure on the bottom wall at the mid-domain cross-section (z = 12.5mm) with the results from the literature is presented in Fig. 3. From the figure, it is evident that the calculated shock system in the cold flow case closely matches the literature results. In the reacting flow case, the positions of shock systems are in good agreement with the literature results, although there are slight

differences in peak pressures between shock waves compared to the literature, with a maximum error of around 4% in the near-field of the injection. Therefore, it can be concluded that the computational methods used in this paper are reasonable and reliable.

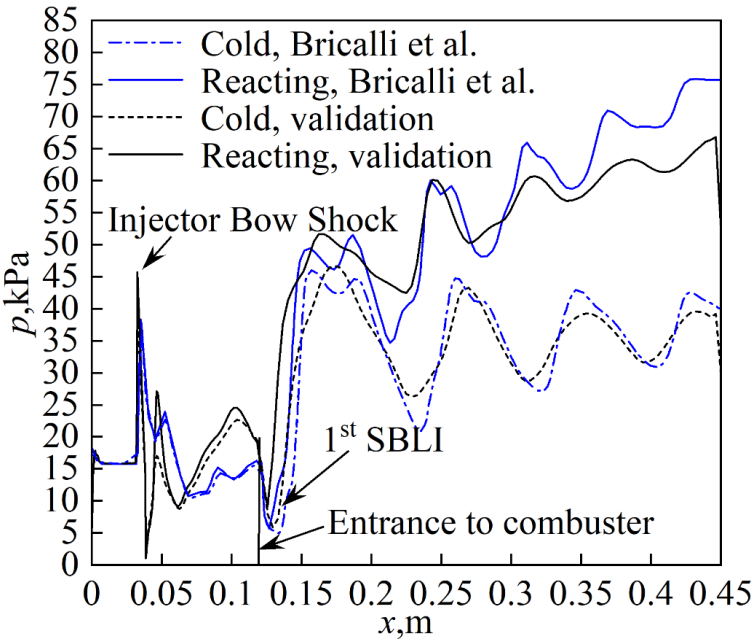

Fig. 3 Comparison of pressure on the bottom wall in the central plane of the computational domain with literature

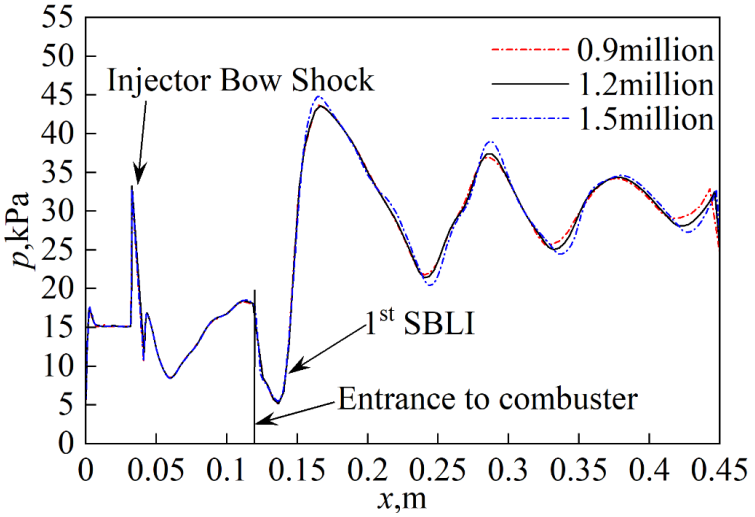

Fig. 4 Pressure on the bottom wall of the central plane (z=12.5mm) in the computational domain

To validate the accuracy of the computational results, grid independence analysis is conducted using three different grid scales, with grid numbers of 0.9million, 1.2 million, and 1.5 million, respectively. Grid convergence is assessed by comparing the time-converged numerical solutions for coarse, medium, and fine grids. Fig. 4 presents a comparison of the bottom wall pressure for the three grid sizes. The pressure data indicate that the positions of shock systems do not vary significantly between each grid. However, there are differences in peak pressure values between shock waves for different grids. Compared to the fine grid, the coarse and medium grids consistently yield peak pressure values approximately 5% and 4% lower, respectively. Additionally, the position of shock systems shifts towards the inlet of the combustor compared to the fine grid. The pressure data suggest that the flow gradually tends towards grid-independent solutions. To save computational costs, the following results are obtained using the medium grid with 1.2 million cells.

3. Results and discussion

3.1. Flow in the thermodynamic equilibrium state

First, thermodynamic equilibrium computations are conducted under non-reacting and reacting conditions, and the results are compared as shown in Fig. 5. Fig. 5a illustrates a comparison of pressure coefficient, indicating a significant increase in pressure due to combustion. As shown in Fig. 5b, the shock structure in the combustion chamber changes with reaction, leading to alterations in the position of shock waves. This change is attributed to the reduction in Mach number caused by the reaction, thereby modifying the shock structure. The pressure coefficient c_p is calculated using the following formula:

$$c_p = (p - p_\infty) / \left(\frac{1}{2}\rho_\infty U_\infty^2\right) \tag{1}$$

where p_∞, ρ_∞, U_∞ represent the pressure, density, and velocity of the far field.

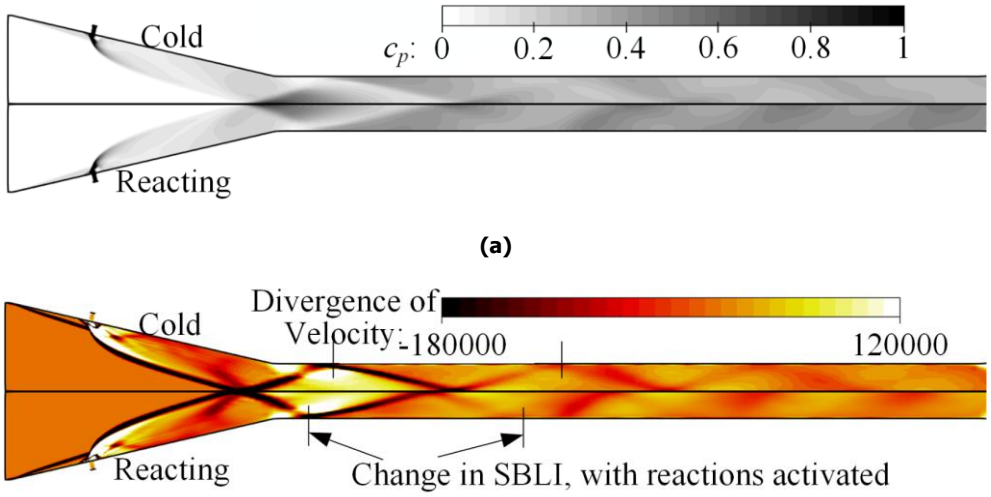

Fig. 5 Thermodynamic equilibrium flow field: (a) injector symmetry plane pressure coefficient contours, (b) injector symmetry plane shock structure described by velocity divergence

3.2. Flow in thermal non-equilibrium state

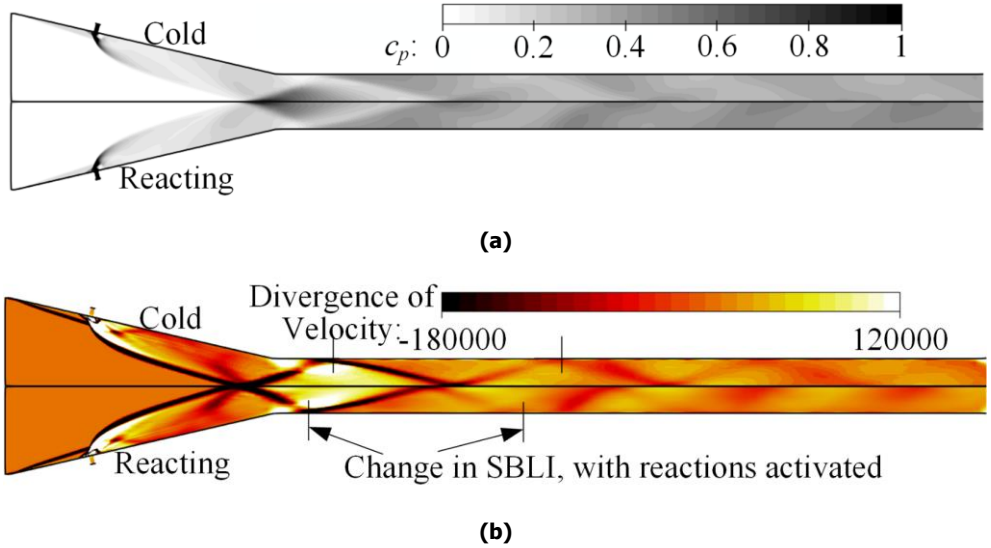

Fig. 6 Non-equilibrium flow field results: (a) injector symmetry plane pressure coefficient contours, (b) injector symmetry plane shock structure described by velocity divergence

The thermodynamic non-equilibrium results obtained using Park's dual-temperature model are shown in Fig. 6. Similar to the thermodynamic equilibrium state, combustion leads to an increase in pressure, and the shock structure changes with the activation of the reaction.

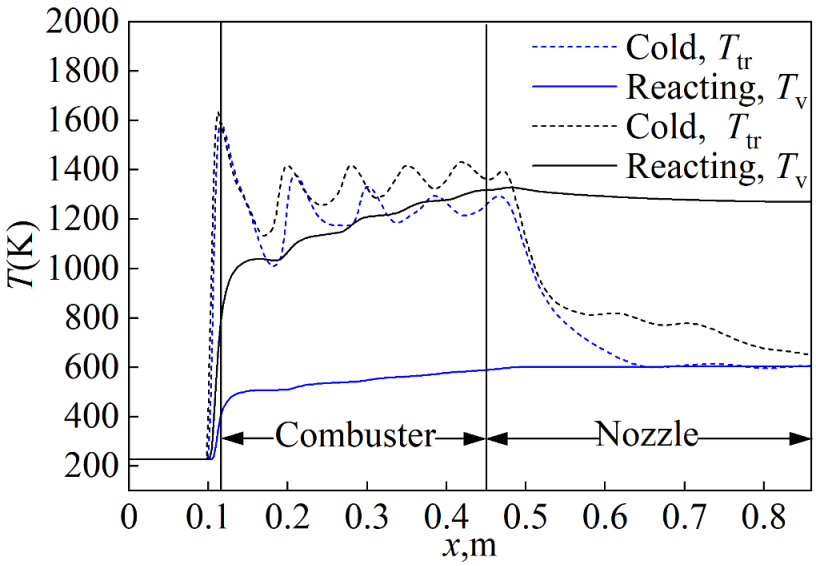

Fig. 7 Temperature distribution close to the top plane

The temperature distributions along the length near the top wall are compared as shown in Fig. 7. For the cold flow case, there are no shock waves encountered at the inlet, and T_{tr} is in thermal equilibrium with T_v. After passing through the shock waves, T_{tr} undergoes a sudden jump, followed by a decrease, resulting in the appearance of five peak temperatures after passing through five shock waves. On the other hand, T_v only increases after the first shock wave, followed by a slow and steady increase. Additionally, it is observed that T_{tr} and T_v are in thermal equilibrium after x = 0.65 m. When a fluid passes through strong discontinuities such as shock waves, a significant amount of kinetic energy is converted into translational motion, causing the thermal equilibrium state between translational-rotational and vibrational modes to be disrupted. Subsequently, this translational motion exchanges energy with rotational, vibrational, and chemical modes through a certain number of collisions [9].

Table 4. Initial conditions

T_{tr}/K	T_v/K	Pressure P/Pa	Molar fraction X_N2	Molar fraction X_O2	Molar fraction X_H2
2000	900	70000	0.69	0.21	0.1

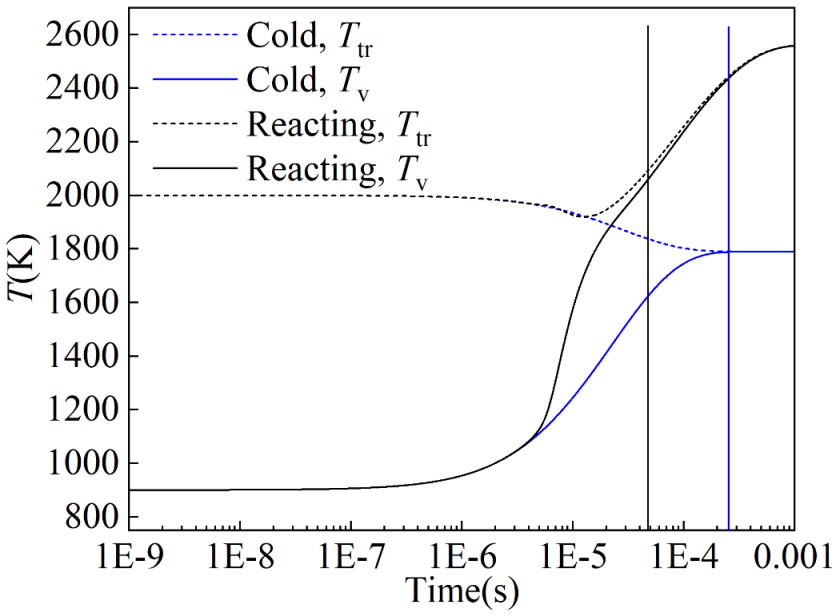

Fig. 8 Results of calculated HeatBath model

For the reacting flow case, it can be observed that T_{tr} exhibits a similar trend to the cold flow case, albeit with higher values, while T_v rises sharply after the first shock wave and does not return to thermal equilibrium with T_{tr} later on. This is related to the relaxation time between vibrational temperature T_v and translational temperature T_{tr} when they reach equilibrium [16]. The V-T relaxation time can be calculated using a thermal bath model. Vatansever et al. [17] pointed out in their paper that there are differences in V-T relaxation time between frozen flow and reacting flow in the thermal bath model calculation. To test the influence of H_2 combustion reaction on the V-T relaxation time in this paper, initial conditions are given as shown in Table 4.

The results of the thermal bath model calculation are shown in Fig. 8, indicating that the H_2 combustion reaction accelerates the translational-vibrational relaxation. Therefore, the results for the reacting flow case can be explained as follows: in the combustion chamber region, the reaction accelerates the V-T relaxation, leading to a rapid increase in vibrational temperature T_v, and each decrease in T_{tr} is accompanied by an increase in T_v. As the flow reaches the nozzle region where the reaction is almost negligible, the V-T relaxation slows down. In the first half of the nozzle, as the flow expands, the temperature T_{tr} decreases significantly, while T_v decreases as well, but not as quickly as T_{tr}, indicating a significant thermodynamic non-equilibrium phenomenon. Subsequently, as the flow velocity increases rapidly, both T_v and T_{tr} enter the frozen state successively, meaning that the temperature values remain essentially constant, eventually resulting in the phenomenon of T_v being higher than T_{tr}.

3.3. Comparison of the non-equilibrium effects

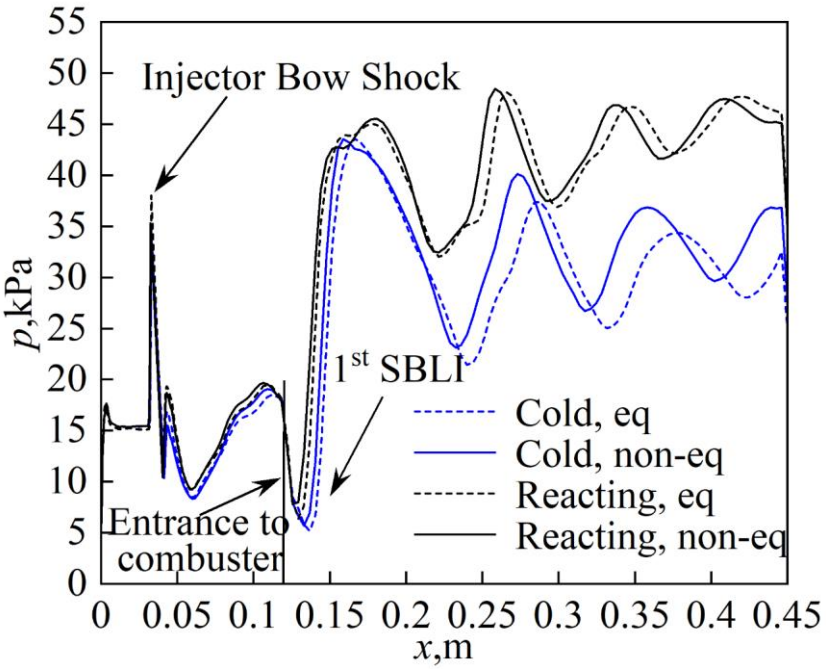

Fig. 9 Comparison of bottom wall pressure across the injector plane (z=12.5mm)

Comparing the pressure near the bottom wall of the central cross-section as shown in Fig. 9, it is evident that the shock positions are closer to the inlet in the non-equilibrium case. Additionally, compared to the equilibrium state, the non-equilibrium effects result in an increase of 7% and 1% in peak pressure for the cold flow and reacting flow cases, respectively. Therefore, compared to the equilibrium state results, non-equilibrium effects lead to a forward shift in shock positions and an increase in peak pressure at the shock waves, with a more pronounced impact on the cold flow.

The comparison of the T_{tr} temperature field is shown in Fig. 10. It can be observed that the temperature calculation results for the non-equilibrium state are slightly higher compared to the equilibrium state. This indicates that thermodynamic non-equilibrium effects lead to a slight increase in T_{tr}. This is because in equilibrium state, T_{tr} is assumed to be in thermal equilibrium with Tv, and when the degree of excitation of vibrational energy is very high, under the condition of constant total energy, the translational-rotational energy in the non-equilibrium state is higher than that in the equilibrium state, resulting in a higher T_{tr}.

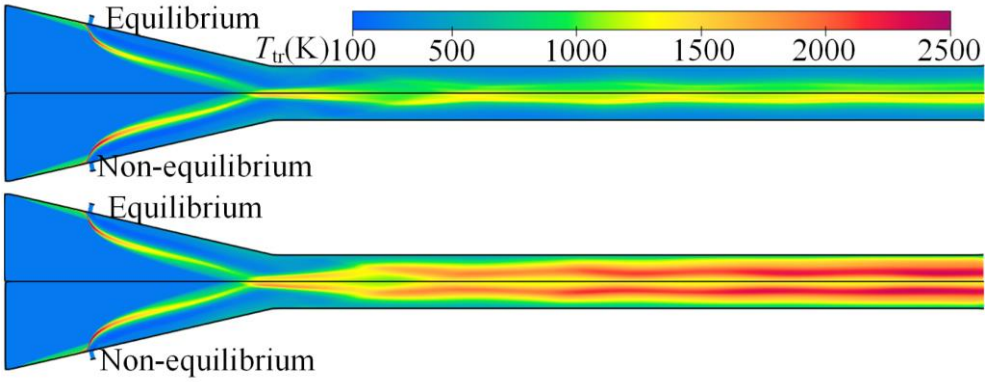

Fig. 10 Comparison of tran-rotational temperature, cold (top) and reacting (bottom)

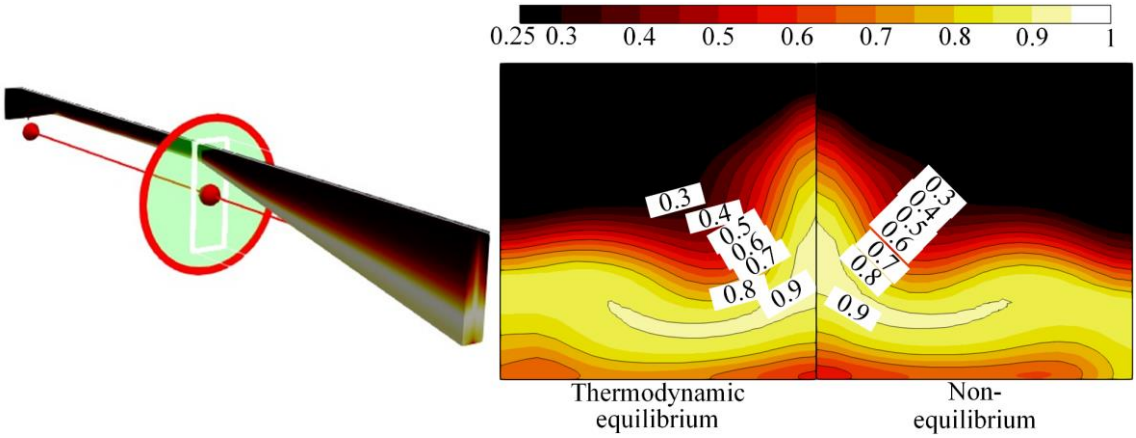

Fig. 11 Combustion efficiency of the exit section of the combustion chamber

The combustion efficiency at the outlet section of the combustion chamber is shown in Fig. 11. Combustion efficiency is defined as the ratio of the actual mass fraction of H_2O to the stoichiometric mass fraction of H_2O. It can be observed that the combustion efficiency for the non-equilibrium case is lower than that for the equilibrium state. This indicates that considering non-equilibrium effects leads to a smaller degree of reaction. Thermodynamic non-equilibrium effects decrease the extent of the reaction because temperature changes affect the movement of chemical equilibrium. With the increase in temperature for exothermic reactions, the chemical equilibrium shifts towards the reverse reaction, reducing the extent of the reaction.

4. Conclusions

This paper conducts numerical simulations for a scramjet engine under flight conditions with a Mach number of 12, considering both thermodynamic equilibrium and non-equilibrium states. The analysis focuses on shock wave patterns, parameter distributions, and combustion performance characteristics within the engine. The concluding remarks are:

1. Thermodynamic non-equilibrium effects have a certain influence on the shock structure position and peak pressure between shock waves in the internal flow field of a scramjet engine. Compared to the results of equilibrium state calculations, the effect of thermodynamic non-equilibrium leads to a forward shift in shock positions and an increase of 7% and 1% in peak pressure between shock waves for the cold flow and reacting flow cases, respectively. This indicates that thermodynamic non-equilibrium effects cannot be ignored in this scenario.
2. Under the condition of consistent total enthalpy at the inlet, thermodynamic non-equilibrium effects affect the translational temperature. For both frozen flow and reacting flow cases, the translational temperature T_{tr} calculated in the non-equilibrium state is slightly higher than that in the equilibrium state. The effect of thermodynamic non-equilibrium leads to a slight increase in T_{tr}.

3. In terms of combustion efficiency, the combustion efficiency at the outlet section of the combustion chamber in the non-equilibrium state is lower, indicating that thermodynamic non-equilibrium effects reduce the extent of the reaction. The increase in translational temperature caused by thermodynamic non-equilibrium effects is the main reason for the decrease in combustion efficiency. Therefore, considering the impact of thermodynamic non-equilibrium effects on engine characteristics is necessary in high-speed numerical simulations and engine structural design.

References

1. Xianliang C, Song F.: Linear stability analysis of hypersonic boundary layer on a flat-plate with thermal-chemical non-equilibrium effects. Acta Acrodynamica Sinica. 38(2), 316–325 (2020)
2. Yuan J Y, Ren X, Cai G B.: Simulation of high temperature gas effects in high enthalpy double cone/wedge flows. Physics of Cases. 7(4), 10–18 (2022)
3. Yang'aoxiao F, Weizhong D, Mingsong D.: Numerical simulation of thermochermical non-equilbrium flow field in arc-jet tunnel. Journal of Experiments in Fluid Mechanics. 33(3), 1–12 (2019)
4. Yue Lianjie, Zhang Xu, Zhang Qifan.: Research progress on high-Mach-number scramjet engine technologies. Chinese Journal of Theoretical and Applied Mechanics. 54(2), 263–288(2022)
5. J. M. A. Longo, K. Hannemann, and V. Hannemann.: The challenge of modeling high speed flows. In Proceedings of the 6th EUROSIM Congress on Modelling and Simulation. Ljubljana, Slovenia, 2007
6. A. Anna.: Numerical Modeling of Surface Chemistry Processes for Hypersonic Entry Environments, PhD thesis, The University of Michigan, Ann Arbor, MI, US, 2013
7. Wentao Xiong.: On Shock-shock Interaction in Double-wedge Flow with High Temperature Non-equilibrium Effects. University of Science and Technology of China, 2017
8. Bricalli, Mathew G.: Scramjet Performance with Nonuniform Flow and Swept Nozzles. AIAA Journal (2018). https://doi.org/10.2514/1.J056963
9. Casseau V, Espinoza D E R, Scanlon T J.: A Two-Temperature OpenSource CFD Model for Hypersonic Reacting Flows. Part Two: Multi-dimensional Analysis. Aerospace (2016). https://doi.org/10.3390/aerospace3040034
10. Casseau V.: An open-source CFD solver for planetary entry. Ph.D.Thesis, Dept. of Mechanical and Aerospace Engineering, Univ. of Strathclyde, Glasgow, Scotland, U.K., 2017
11. L. Landau and E. Teller.: Theory of sound dispersion. Physikalische zeitschrift der Sowjetunion. 10, 34-43(1936)
12. Menter F R, Kuntz M, Langtry R.: Ten years of industrial experience with the SST turbulence model. Turbulence, heat and mass transfer. 4(1), 625-632(2003)
13. Ó Conaire M, Curran H J, Simmie J M..: A Comprehensive Modeling Study of Hydrogen Oxidation. International Journal of Chemical Kinetics (2004). https://doi.org/10.1002/-kin.20036
14. Ao Y, Wu K, Lu H..: Combustion dynamics of high Mach number scramjet under different inflow thermal nonequilibrium conditions. Acta Astronautica (2023). https://doi.org/10.1016-/j.actaastro.2023.04.020
15. Bricalli M G, Brown L M, Boyce R R.: Numerical Investigation into the Combustion Behavior of an Inlet-Fueled Thermal-Compression-Like Scramjet. AIAA Journal (2015). https://doi.org-/10.2514/1.J053513
16. Bai Hezhi, Chen Bing, Xu Xu.: Numerical Simulation of Hypersonic Nozzle Flow in Thermochemical Nonequilibrium Based on Parabolized Navier-Stokes Equation. Tactical Missile Technology (2018). https://doi.org/10.16358/j.issn.1009-1300.2018.7.197

17. D. Vatansever, B. Çelik.: An Open-Source Hypersonic Solver For Non-equilibrium Flows. Journal of Aeronautics and Space Technologies. 14(1), 35-52(2021)